



The Complete Calibration of the Color–Redshift Relation (C3R2) Survey: Analysis and Data Release 2

Daniel C. Masters¹ , Daniel K. Stern¹ , Judith G. Cohen² , Peter L. Capak³ , S. Adam Stanford⁴, Nina Hernitschek² , Audrey Galametz⁵, Iary Davidzon⁶ , Jason D. Rhodes^{1,11} , Dave Sanders⁷ , Bahram Mobasher⁸, Francisco Castander^{9,10} ,

Kerianne Pruet⁴, and Sotiria Fotopoulou¹²

¹ Jet Propulsion Laboratory, California Institute of Technology, Pasadena, CA 91109, USA

² California Institute of Technology, Pasadena, CA 91125, USA

³ Spitzer Science Center, Pasadena, CA 91125, USA

⁴ Department of Physics, University of California, Davis, CA 95616, USA

⁵ Department of Astronomy, University of Geneva, 1205, Versoix, Switzerland

⁶ Infrared Processing and Analysis Center, California Institute of Technology, Pasadena, CA 91125, USA

⁷ Institute for Astronomy, University of Hawaii, 96822, USA

⁸ Department of Physics and Astronomy, University of California, Riverside, CA 92521, USA

⁹ Institut d'Estudis Espacials de Catalunya (IEEC), E-08034 Barcelona, Spain

¹⁰ Institute of Space Sciences (ICE, CSIC), Campus UAB, Carrer de Can Magrans, s/n, E-08193 Barcelona, Spain

¹¹ Kavli Institute for the Physics and Mathematics of the Universe (IPMU), Tokyo, Japan

¹² Center for Extragalactic Astronomy, Department of Physics, Durham University, Durham, UK

Received 2018 November 30; revised 2019 March 19; accepted 2019 April 3; published 2019 May 28

Abstract

The Complete Calibration of the Color-Redshift Relation (C3R2) survey is a multi-institution, multi-instrument survey that aims to map the empirical relation of galaxy color to redshift to $i \sim 24.5$ (AB), thereby providing a firm foundation for weak lensing cosmology with the Stage IV dark energy missions *Euclid* and *WFIRST*. Here we present 3171 new spectroscopic redshifts obtained in the 2016B and 2017A semesters with a combination of DEIMOS, LRIS, and MOSFIRE on the Keck telescopes.¹³ The observations come from all of the Keck partners: Caltech, NASA, the University of Hawaii, and the University of California. Combined with the 1283 redshifts published in DR1, the C3R2 survey has now obtained and published 4454 high-quality galaxy redshifts. We discuss updates to the survey design and provide a catalog of photometric and spectroscopic data. Initial tests of the calibration method performance are given, indicating that the sample, once completed and combined with extensive data collected by other spectroscopic surveys, should allow us to meet the cosmology requirements for *Euclid*, and make significant headway toward solving the problem for *WFIRST*. We use the full spectroscopic sample to demonstrate that galaxy brightness is weakly correlated with redshift once a galaxy is localized in the *Euclid* or *WFIRST* color space, with potentially important implications for the spectroscopy needed to calibrate redshifts for faint *WFIRST* and LSST sources.

Key words: astronomical databases – catalogs – cosmology: observations – galaxies: distances and redshifts – surveys

Supporting material: machine-readable table

1. Introduction

Stage IV cosmology missions (LSST, *Euclid*, and *WFIRST*) will use deep imaging of billions of galaxies in filters spanning the optical to the near-infrared to estimate photometric redshifts (photo- z s) for weak lensing cosmology. While high-quality photo- z s are also crucial for many other investigations, the photo- z requirements for cosmology are particularly stringent. Weak lensing cosmology requires unbiased redshift estimates (Huterer et al. 2006; Ma et al. 2006), at a level that is not possible with classical photo- z estimation techniques such as spectral template fitting. For *Euclid* and *WFIRST*, the requirement is usually given that the mean redshift $\langle z \rangle$ of galaxies in ~ 10 shear bins must be known to better than 0.2% (that is, $\Delta\langle z \rangle \leq 0.002(1 + \langle z \rangle)$ for each bin). Numerous tests have shown that this level of accuracy is not achieved with traditional algorithms and realistic training samples. The bias requirement, in particular, makes spectroscopic calibration

samples necessary for the success of these missions (Newman et al. 2013).

Stage III cosmology surveys currently underway also face the photo- z estimation challenge, and constitute an important testbed for the photo- z techniques to be employed in the Stage IV experiments. These include the Kilo-Degree Survey (de Jong et al. 2015, 2017; Hildebrandt et al. 2017), the Dark Energy Survey (DES Collaboration et al. 2018; Troxel et al. 2018), and the Hyper-Suprime Cam Survey (Aihara et al. 2018). A variety of techniques have been employed in these surveys to constrain redshift distributions, $N(z)$, of galaxies in shear bins—from template fitting (e.g., Benítez 2000; Brammer et al. 2008; Ilbert et al. 2009), to machine learning techniques based on training samples (e.g., Collister & Lahav 2004; Carrasco Kind & Brunner 2013), and clustering redshifts that use the spatial distribution of overlapping spec- z samples to infer the $N(z)$ distribution of the photometric sample (e.g., Newman 2008; Ménard et al. 2013; McQuinn & White 2013; Schmidt et al. 2013; Morrison et al. 2017). Re-weighting of the spectroscopic sample to better match the photometric sample, as described in Lima et al. (2008), has also been used. It is

¹³ Redshifts and spectra released by C3R2 to date can be found at <https://sites.google.com/view/c3r2-survey/home> and <https://koa.ipac.caltech.edu/Datasets/C3R2>.

generally agreed that a key limitation is the need for a fully representative training sample of spec-*z*s that explores the range of galaxy properties present in the surveys.

The Complete Calibration of the Color-Redshift Relation (C3R2) survey (Masters et al. 2017, hereafter M17) was initiated in response to this need, with the goal of mapping the empirical relation between galaxy redshift and color to the *Euclid* depth of $i \sim 24.5$ (AB). The survey strategy is based on the fact that the manifold of observed galaxy colors to a given survey depth is both limited and measurable. Moreover, we make the (testable) assumption that there exists a well-defined, mostly non-degenerate relation between a galaxy’s position in multi-color space and its redshift, which can be discovered empirically. Uncovering this $P(z|C)$ relation is the goal of the C3R2 survey.

The C3R2 survey strategy follows the method outlined in Masters et al. (2015, hereafter M15). M15 illustrated the use of an unsupervised manifold learning algorithm, the self-organizing map (SOM; Kohonen 1982), to map the color distribution of galaxies in the high-dimensional color space ($u - g, g - r, \dots, J - H$) anticipated for *Euclid* and *WFIRST* photo-*z* estimation. This high-dimensional mapping allows us to directly determine which parts of galaxy color space are well sampled with existing spectroscopy and which are not, thus letting us focus spectroscopic calibration effort on those regions that are the least constrained. Essentially, we seek to obtain the minimum additional spectroscopy needed to build a representative training sample, such that direct inference of the $P(z|C)$ relation can be made sufficiently accurate to meet the cosmology requirements.

In M17 we presented the results of the first five nights of C3R2 observations taken in the 2016A semester. Here we present results obtained in the 2016B and 2017A semesters, comprising 23.5 Keck nights, of which ~ 14 had good observing conditions. These nights were allocated as part of a multi-institution effort to solve the redshift calibration problem for *Euclid* and make significant progress toward the *WFIRST* calibration, with time coming from all Keck partners: Caltech (10 nights, PI J. Cohen), NASA (five nights, PI D. Stern), University of Hawaii (six nights, PI: D. Sanders), and the University of California (2.5 nights, PI: B. Mobasher). A parallel effort with the Very Large Telescope (PI: F. Castander) is also underway, the results of which will be presented in a separate data release. We refer the reader to M15 for background on the calibration approach and to M17 for more details on the C3R2 survey.

This paper is structured as follows. In Section 2 we describe the development of homogeneous photometric catalogs in $ugrizYJHK_s$ for multiple deep fields. In Section 3 we describe updates to the survey strategy. In Section 4 we describe the observations and data reductions of the 2016B/2017A observations. In Section 5 we present our spectroscopic results from 23.5 nights in 2016B/2017A, and discuss the performance of the method. In Section 6 we investigate the status of the calibration effort, and issues still to be addressed.

2. Constructing a Uniform Color System for Multiple Deep Fields

Conducting the C3R2 survey across multiple fields at different right ascensions lets us take full advantage of observing nights and helps mitigate the effect of cosmic variance in an individual field. However, the sensitive multi-color selection technique we

Table 1
Overview of the Deep Fields Targeted by C3R2 in DR2

Field	R.A. (J2000)	Decl. (J2000)	Area (deg ²)	Optical Data (<i>ugriz</i>)	Near-IR Data (<i>YJHK_s</i>)
VVDS-2h	02 ^h 26 ^m	−04° 30′	1.0	CFHTLS	VISTA
COSMOS	10 ^h 00 ^m	+02° 12′	2.0	CFHTLS	VISTA
EGS	14 ^h 19 ^m	+52° 41′	1.0	CFHTLS	CFHTLS- WIRDS ^a

Note.

^a *Y* band obtained from CFHT-WIRCAM observations separate from the WIRDS survey.

employ requires very homogeneous photometry between fields. The fields that can be used for C3R2 targeting are thus limited to those with uniform, well-calibrated photometry spanning the optical to near-infrared (near-IR), to depths comparable to or deeper than the planned *Euclid* survey.

We determined that the fields currently meeting this criterion are the Canada–France–Hawaii Telescope Legacy Survey¹⁴ (CFHTLS) deep fields (uniform MegaCam *ugriz* imaging to AB point source depths of 26.3, 26.0, 25.6, 25.4, 25.0, respectively), which also have VISTA or CFHT-WIRCAM Deep Survey (WIRDS; Bielby et al. 2012) near-IR imaging to the *Euclid* depth of $YJH \sim 24$ AB (5σ) (Table 1). These fields are VVDS-2h (McCracken et al. 2003; Le Fèvre et al. 2004; Jarvis et al. 2013), COSMOS (Capak et al. 2007; Scoville et al. 2007; McCracken et al. 2012), and EGS (Davis et al. 2007). In preparation for 2016B/2017A observations, we brought the near-IR photometry from these three deep fields onto a consistent *Euclid*/*WFIRST*-like color system and collected existing redshifts from the literature.¹⁵

SXDS, CDFS, and GOODS-N were not included in our primary targeting because they lack the highly uniform photometry we believe is needed. However, all of these fields have extensive spectroscopy that can be added to the color–redshift relation with a rough color conversion to the *Euclid*-like system.

2.1. Homogenizing the Near-infrared Photometry

Matching galaxy photometry from multiple fields at the desired level of precision is non-trivial because of the different instruments, filters, and photometry techniques employed in deep surveys. Fortunately, the CFHTLS deep field imaging of VVDS-2h, COSMOS and EGS in CFHT MegaCam *ugriz* is already highly uniform, which we confirmed by comparing the colors (measured with 2'' aperture photometry) of stars in each field in various color–color diagrams.

That left only the problem of deriving matched near-IR photometry for the fields. The CFHTLS-WIRDS survey (Bielby et al. 2012) obtained homogenized photometry for CFHT MegaCam optical and WIRCam near-IR (JHK_s) imaging in these fields. However, subsequent VISTA imaging in VVDS-2h and COSMOS is both deeper than CFHTLS-WIRDS and

¹⁴ <http://www.cfht.hawaii.edu/Science/CFHTLS/>

¹⁵ Note that the photometry from these fields is not corrected for galactic extinction. However, this correction is non-trivial because it is SED-dependent; moreover, the galactic extinction for these deep fields is low. Ultimately, we will want to apply a galactic extinction correction based on the method developed in Galametz et al. (2017).

includes the Y band. Our goal, therefore, was to bring the VVDS-2h and COSMOS VISTA observations onto the CFHTLS-WIRDS color system. We now describe the steps taken to accomplish this.

2.1.1. VVDS-2h

To bring the VISTA data in VVDS-2h onto the CFHTLS-WIRDS system, we first needed to align the VISTA observations to the astrometric system of CFHTLS. We used the SCAMP and SWarp packages (Bertin et al. 2002; Bertin 2006) to compute and apply the needed astrometric correction to the VISTA imaging. The VISTA photometry was then extracted in an identical way as the CFHTLS-WIRDS data using the Bielby et al. (2012) gri detection images and SExtractor settings. A zero-point offset was then applied to the VISTA photometry to match WIRDS. No filter-dependent corrections were required because the filters of VISTA and CFHT-WIRCam are almost identical.

2.1.2. COSMOS

The COSMOS field has been the subject of extensive imaging spanning the electromagnetic spectrum, including from CFHTLS and UltraVISTA (McCracken et al. 2012). The VISTA imaging from UltraVISTA is already on the same astrometric system as the CFHTLS data. As with VVDS-2h, we re-extracted the COSMOS UltraVISTA photometry using the same gri detection images and SExtractor settings as the CFHTLS-WIRDS survey. A zero-point correction was derived and applied to match the UltraVISTA photometry to CFHTLS-WIRDS.

2.1.3. EGS

EGS has not been observed with VISTA, as it is too far north. Therefore, for this field we used the JHK_s near-IR catalogs from CFHTLS-WIRDS directly. CFHTLS-WIRDS does not include Y observations, so we downloaded archival Y imaging from the CFHT Science Archive. We generated mosaics using SCAMP and SWarp on the output of the pipeline process data from the Canadian Astronomy Data Centre. We then extracted the photometry with SExtractor using the CFHTLS gri detection image. Finally, we used the measured stellar locus in colors involving Y band to force the reduced EGS Y photometry to match the COSMOS data. Of the three fields, the color system for EGS is the least robust, due to the lower depth of the CFHTLS-WIRDS data compared with VISTA, as well as the suboptimal Y -band data.

2.2. Validation of the Photometry

We examined star colors in a range of color-color diagrams to validate the photometry between fields. Stars were selected from each field using the cut in r -band magnitude versus half-light radius shown in Figure 1. The example color-color plots shown in Figure 2 illustrate the color uniformity across broad wavelength baselines. The stellar loci align well, with residual offsets at the $\lesssim 0.02$ mag level, which is a sub-resolution of the SOM used for targeting. Moreover, we examined the spread of galaxy colors in each field with the well-known g_zK_s diagram (Figure 3). Again, we see good agreement between fields. We therefore have confidence that galaxies in each field can be compared on the same color system.

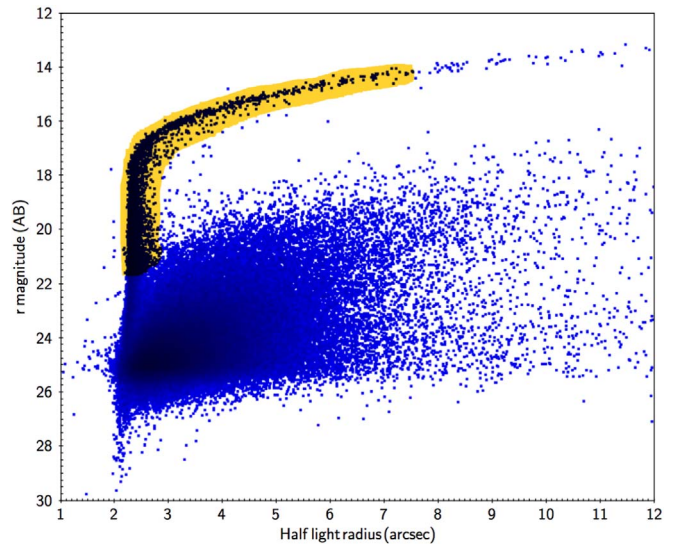


Figure 1. Selection used to define the stellar locus for each field. The locus is clear in this plot of r -band magnitude vs. half-light radius; the highlighted region illustrates our selection. We select stars in the magnitude range $14 \lesssim r \lesssim 22$ to test the uniformity of the color system.

3. Revised Target Selection Procedure

In general, it is not possible to populate spectroscopic slitmasks (covering ~ 50 arcmin² of sky) exclusively with galaxies that are both important for photo- z calibration and will yield secure redshifts with a given observational setup. We therefore developed a priority scheme that weights galaxies first according to their usefulness for photo- z calibration, and then sorts based on the probability of obtaining a secure redshift for a planned observation, to maximize survey efficiency. The selection is ultimately based on the revised color map, which we now describe.

3.1. Updated Self-organized Map

We regenerated a self-organizing map to use as the basis for C3R2 targeting and analysis from the homogenized deep field photometry from VVDS-2h, COSMOS, and EGS. Projections of the new SOM are shown in Figure 4. The structure is similar (by design) to the SOM presented in M15 and used in M17. To generate this SOM, we initialized the algorithm with weight vectors from the previous SOM, and tuned down the responsiveness of the algorithm (learning rate function and neighborhood function) in order to preserve the previous structure as much as possible, while faithfully representing the data in the updated color system. For this SOM we included the K_s filter. After the SOM was generated, we tested it by measuring the quantization error—i.e., the typical color offset of a given galaxy from its best-matching cell. As in M15, we find an average Euclidean distance of a galaxy from its best-fit cell in the map of ~ 0.2 mag, meaning that the individual colors of galaxies in the sample are typically offset from the colors of their best-matching cell in the SOM by $\lesssim 0.07$ mag.

3.2. Revised Target Weighting Scheme

We begin with catalogs of uniform photometry in VVDS-2h, COSMOS and EGS, along with all available spectroscopic redshifts from these fields. Each galaxy in the catalogs was then matched to its best-fit SOM cell based on its photometry—i.e., it was assigned to the SOM cell whose weight vector its colors

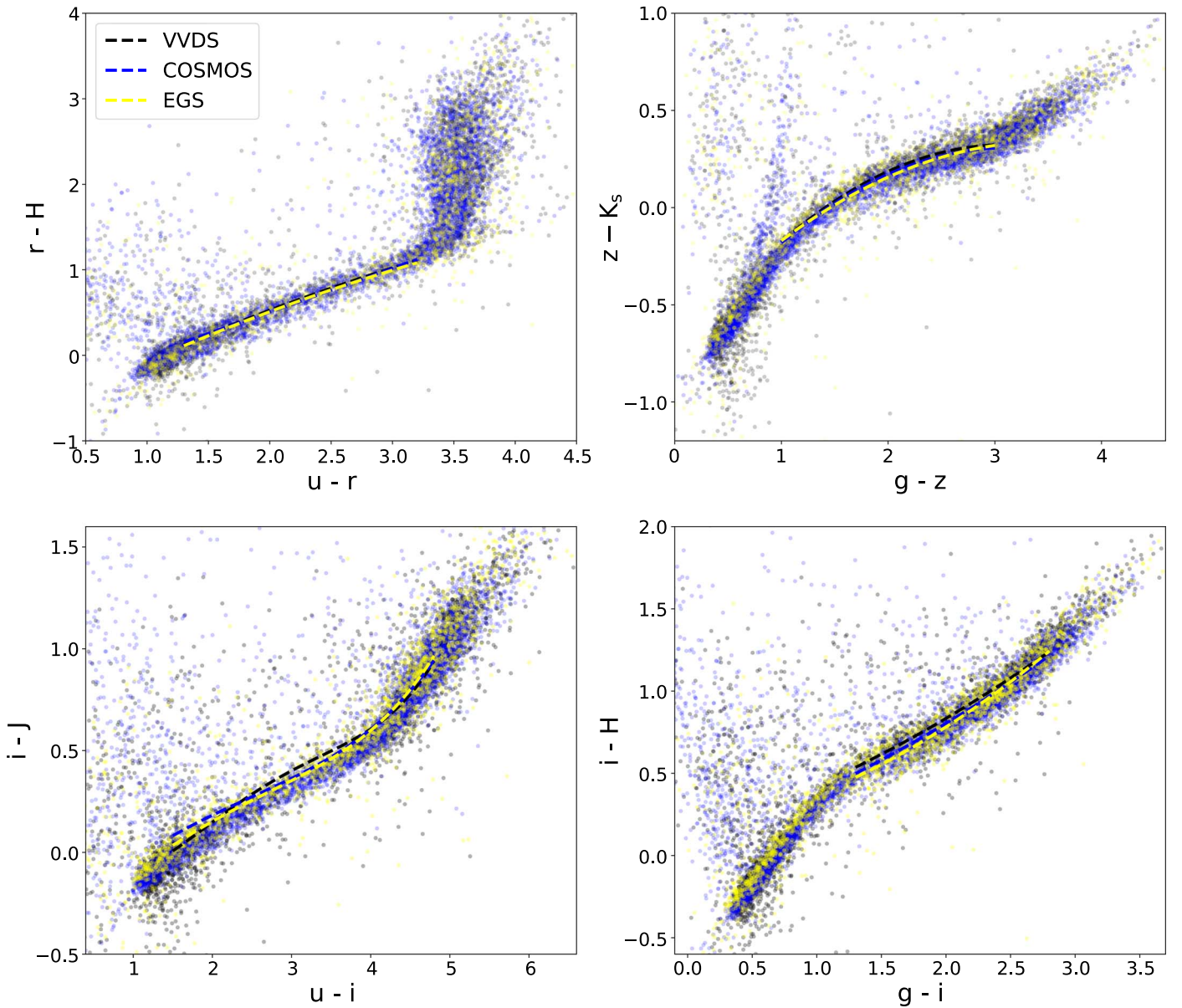


Figure 2. Using stars selected from the three key fields (COSMOS, VVDS-2h, and EGS), we examine the stellar locus in different color-color plots spanning the optical to the near-IR, illustrating the overall excellent color agreement of the fields. This agreement is a necessary condition to employ a sensitive multi-color selection across different fields. In general the loci agree to $\lesssim 0.02$ mag, as confirmed with the low-order polynomial fits shown. The largest residual offsets we find are between the VVDS-2h and COSMOS/EGS fields in the lower left plot ($u-i$ vs. $i-J$), at the $\lesssim 0.05$ mag level. The sources that scatter off the locus in these diagrams are primarily a combination of AGN and non-main-sequence stars.

most closely resemble. This sorting of galaxies on the SOM by color lets us develop a picture of where (in galaxy multi-color space) we have spectroscopy and where it is lacking.

We then cycle through each SOM cell to set priorities for sources in that cell. First we identify existing spectroscopic redshifts in the color cell, as well as existing but currently unanalyzed C3R2 spectra for sources in the cell. Sources with a previous redshift measurement or an unanalyzed C3R2 spectrum are given a priority of zero. The algorithm used to set priorities for the rest of the sources is then as follows:

1. Set the source’s initial priority based on the level of existing spectroscopic coverage for its color cell, increasing the priority as the quality of spectroscopic coverage diminishes:

- (a) If there is at least one high-confidence redshift in the cell already: initial weight = 1.
 - (b) Low/medium-quality redshift and an unanalyzed C3R2 spectrum: initial weight = 2.
 - (c) Low/medium-quality redshift in cell: initial weight = 5.
 - (d) Unanalyzed C3R2 spectrum in cell: initial weight = 7.
 - (e) Neither existing redshifts nor unanalyzed C3R2 spectra in cell: initial weight = 15.
2. Divide weight by two if the object is a poor match to the colors represented by the cell. Specifically, do this if the Euclidean distance between the colors of the object and the cell is greater than 0.3 mag ($\sim 30\%$ of sources are color outliers at this level, corresponding to an average color difference of ~ 0.1 mag in individual colors.) This step is done to avoid calibrating with sources with “unrepresentative” colors.

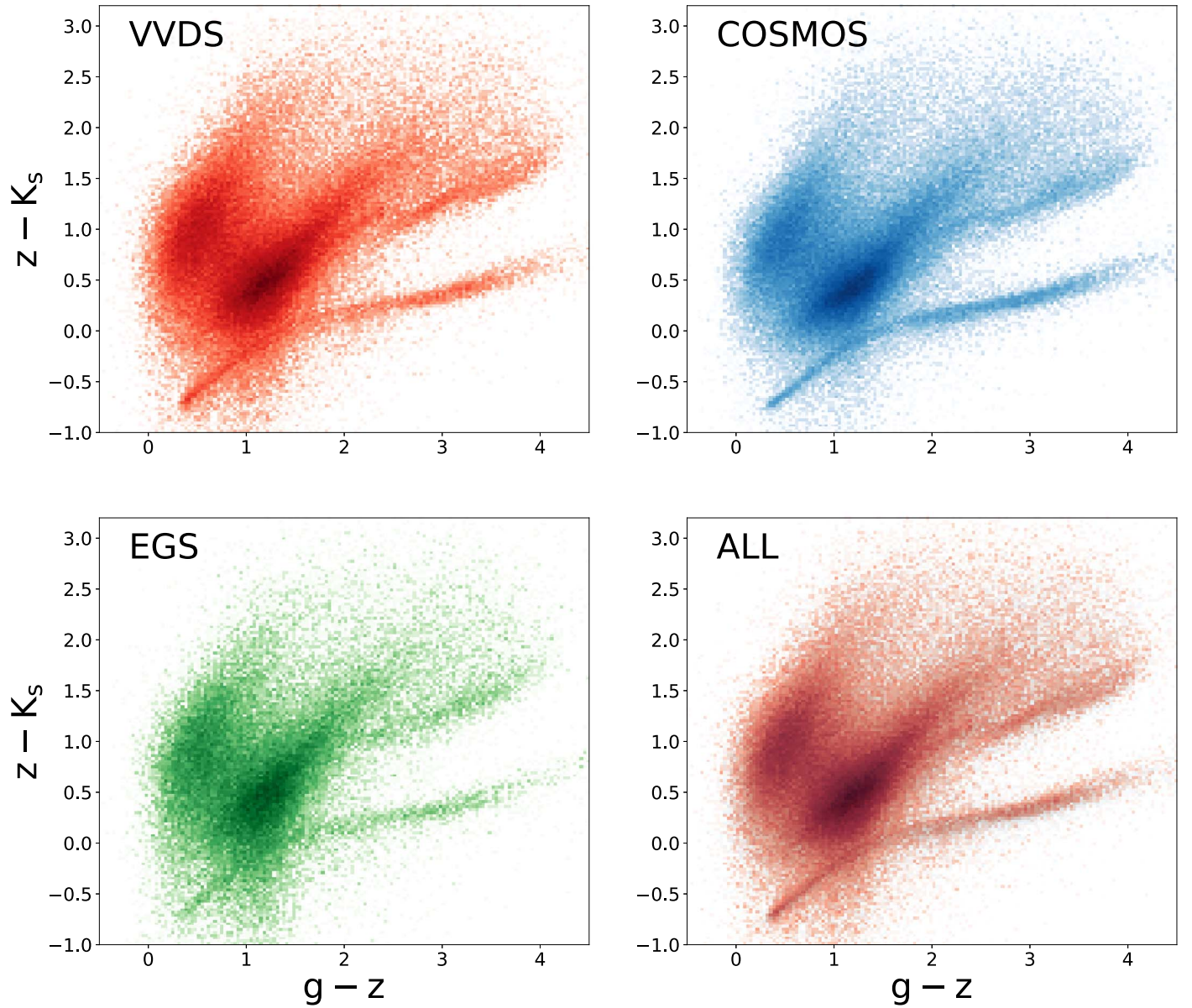


Figure 3. Comparison of galaxy colors in the three C3R2-targeted fields in the gzK_s diagram. This figure illustrates the overall close uniformity of galaxy colors (in addition to the stellar colors) between the three fields. In the bottom right figure we have overlaid the distributions with increasing transparency; essentially no significant difference is apparent.

3. Penalize objects missing two or more bands of photometry by dividing the weight by the number of missing bands.
4. Boost for color cell occupation. First quartile (those color cells with the lowest number of galaxies): multiply object weight by 100; second quartile: multiply by 150; third quartile: multiply by 200; fourth quartile (those color cells with the highest number of galaxies): multiply by 250.
5. Further down-weight sources in cells with multiple reliable redshifts by dividing the weight by the number of reliable redshifts in the color cell.

The criteria described above are chosen to focus on well-populated color cells with little or no existing spectroscopy. Finally, once this priority scheme is applied, we break the catalog up into sources that can be expected to yield redshifts with different instrument/exposure times. For example, for a planned one-hour MOSFIRE H -band observation, we consider sources with expected required integration time <2 hr to be the top tier,

and put them on the mask first. Sources predicted to take longer would be included in a second tier of the mask design. The predicted required exposure times are estimated with an exposure time calculator (written by P. Capak) taking into account the modeled detailed spectral characteristics of each source as well as the instrument sensitivity. For each galaxy we have a predicted type (star-forming, quiescent, or somewhere in between) and redshift from spectral energy distribution fitting. We can thus predict the strongest spectral feature that should be present for a given spectroscopic setup, and set a reasonable continuum signal-to-noise ratio (S/N) threshold for the feature to yield a firm redshift.¹⁶ A variety of mask exposure times (from 1 to 6 hr) were employed to ensure that we would be sensitive to the range of sources in the high-priority sample.

¹⁶ The exposure time estimation is explained in more detail in the Appendix of M15.

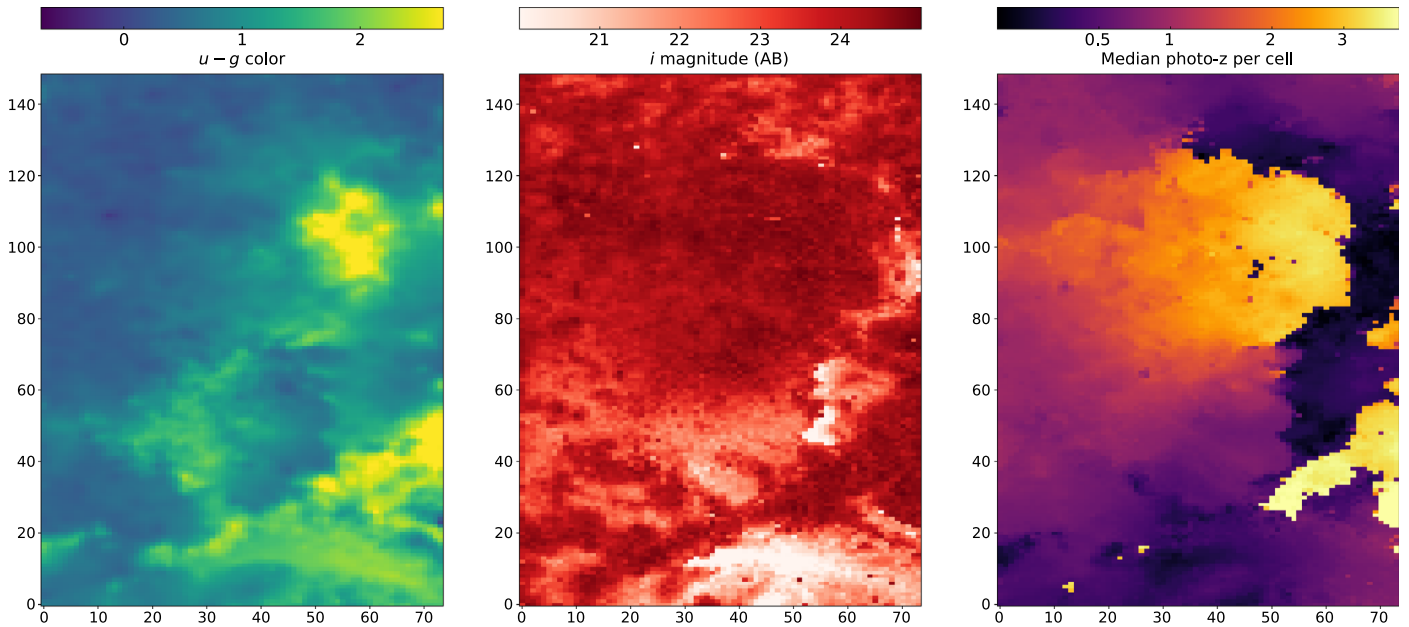


Figure 4. Illustration of the updated self-organized map (SOM) used for the C3R2 DR2 source selection and analysis. Each cell of the SOM represents a particular spectral energy distribution (SED) that shows up with regularity in the deep field data. The axes should be thought of as indices to parts of the high-dimensional galaxy color space. Left: the map colored according to one of the features it encodes, namely the $u - g$ color. Middle: the map colored according to the median i -band magnitude of galaxies occupying each cell. It is clear that the typical magnitude is strongly color-dependent. Right: the SOM colored by the median photometric redshift of galaxies occupying each cell. Note the topological nature of the SOM: similar SEDs group together, producing relatively smooth variation of photo- z with position on the map.

4. Observations and Data Reductions

The observations were conducted from 2016 September to 2017 April. The instruments used are summarized in Table 2. The observing nights and weather conditions are summarized in Table 3. The observed slitmasks are summarized in the Appendix.

4.1. Description of Observations

Observations in 2016B/2017A were conducted largely as described in M17 for the DR1 data. Here we give a brief overview of the observations and reductions.

4.1.1. DEIMOS

DEIMOS observations were conducted using the 600 groove mm^{-1} grating blazed at 7200 Å and the GG400 blocking filter, with dithering performed to improve sky subtraction. We settled on a minimum slit length of 8" as a balance between maximizing the number of targets on the mask and getting good sky measurements. Data were reduced using a modified version of the DEEP2 pipeline designed to deal with dithered data.

4.1.2. MOSFIRE

MOSFIRE was used in its default configuration. For instrumental details we refer the reader to Steidel et al. (2014). For our H -band observations we used integration times of 120 s with ABAB dithering to improve sky subtraction. Reductions were performed with the MOSFIRE Data Reduction Pipeline made available by the instrument team.¹⁷ We chose to observe only in H band because we discovered that the density of high-priority targets for which we could expect to get a secure redshift was notably higher in this band.

¹⁷ <https://keck-datareductionpipelines.github.io/MosfireDRP/>

Table 2
Instruments and Wavelength Coverage

Instrument	Wavelength Range ^a (μm)	Multiplex
DEIMOS	0.5–1.0	~90
LRIS	0.32–1.0	~25
MOSFIRE H	1.45–1.8	~25

Note.

^a Coverage varies somewhat from object to object. These numbers are typical.

4.1.3. LRIS

We used the 400 groove mm^{-1} blue grism blazed at 3400 Å and the 400 groove mm^{-1} red grating blazed at 8500 Å, with the D560 dichroic. Our choice of blue grism gives high sensitivity at bluer wavelengths where spectral features are likely to be found for objects with photometric redshifts of $z \sim 1.5$ –3, while the red coverage allows for the detection of [O II] $\lambda 3727$ for some sources out to $z \sim 1.6$. The LRIS spectra were reduced using the IRAF-based BOGUS software developed by D. Stern, S. A. Stanford, and A. Bunker, and flux-calibrated using observations of standard stars from Massey & Gronwall (1990) observed on the same night using the same instrument configuration.

4.2. Redshift Determination

We refer the reader to M17 for a detailed description of the redshift determination procedure, as well as the quality flags and failure codes we adopt. Briefly, each observed source was assessed independently by two coauthors to determine the redshift and associated quality flag ($Q = 0$ –4, with 4 being certainty), and any conflicts were reconciled through a joint review of the spectra with the help of a third, independent

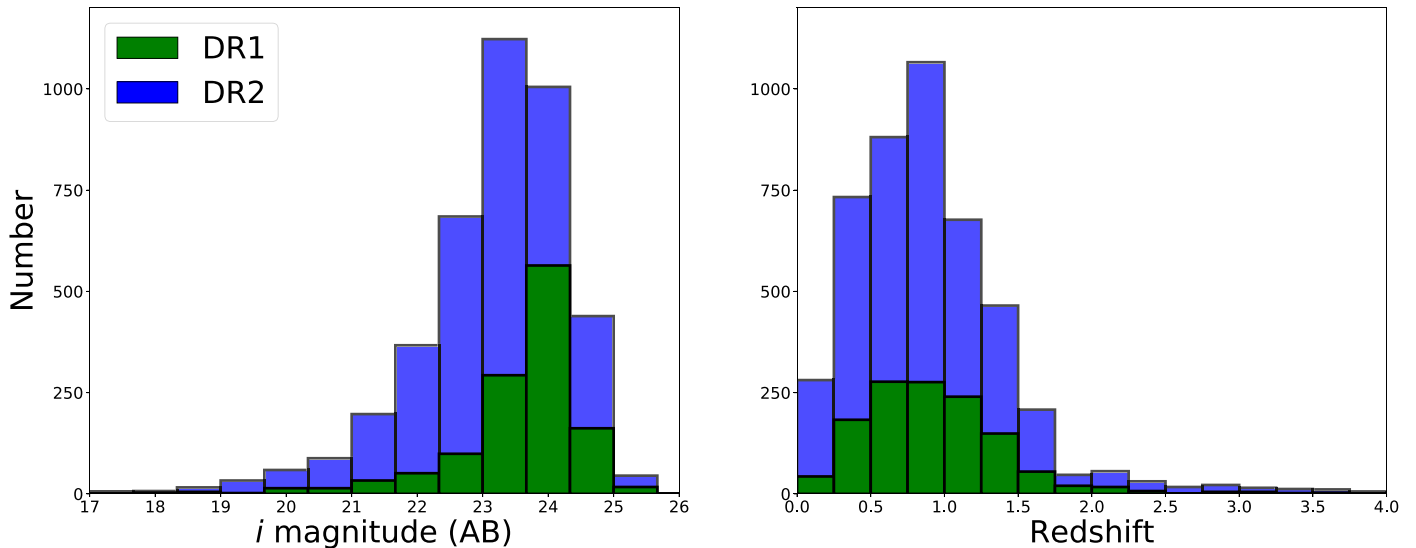


Figure 5. Magnitude and redshift distributions for the C3R2 spectroscopic survey.

reviewer. Sources for which we failed to identify a redshift were assigned failure codes to indicate the most likely reason:

1. Code = -91 : insufficient S/N;
2. Code = -92 : well-detected but with no discernible features;
3. Code = -93 : problem with the reduction;
4. Code = -94 : missing slit (essentially an extreme case of -93).

As in M17, we also investigated all $Q = 4$ (highest quality) sources for which the spectroscopic redshift (z_s) was highly discrepant from the expected photometric redshift. Specifically, we investigated all sources with $|z_p - z_s|/(1 + z_s) \geq 0.15$. The results are presented in Section 5.4.

5. Redshift Results

Out of 4407 targeted sources in DR2, we find a high-confidence ($Q \geq 3$) redshift for 2809, for an overall success rate of 64%. If we consider only the photometric observing nights, our success rate is $\sim 70\%$. We also obtained redshifts for 433 serendipitous sources, for a total of 3242 high-quality redshifts in this release. Some of these (71) are unintentional duplicate observations (see Section 5.3), therefore the total number of unique redshifts released is here is 3171. Combined with the 1283 sources published in M17, the survey to date has obtained and published 4454 redshifts. The magnitude and redshift distributions of the C3R2 sample are given in Figure 5. The C3R2 redshift catalog is provided in a machine-readable table in the Appendix.

5.1. Redshift Performance of the SOM Technique

As a first-order test of the SOM-based calibration method, we assign all galaxies in our spectroscopic sample (DR1+DR2) a photo- z estimate based entirely on their position on the SOM. First, every cell in the SOM is assigned a “calibrated” redshift based on the median photo- z of all galaxies occupying that cell, where the photo- z s come from the literature (Ilbert et al. 2006; Laigle et al. 2016). This calibrated SOM map is illustrated in the right panel of Figure 4.

Galaxies are then assigned a SOM-based redshift point estimate (a “SOMz”) according to which SOM cell they belong to. Note that no spectroscopic information is directly used in calibrating the map at this stage; the calibration is based on averaging photo- z estimates (which may come from data with more bands/higher dimensionality, as with the COSMOS 30-band photo- z estimates) at each point in the *Euclid*/*WFIRST* color space.

With our “gold” sample ($Q = 4$) redshifts from DR1+2 we get the results shown in Figure 6. The outlier fraction, defined as those sources with $|z_p - z_s|/(1 + z_s) > 0.15$, is 4.1%. The scatter estimated using the normalized median absolute deviation (σ_{NMAD}) is 2.3%. The overall bias of the sample (after removing outliers) is -0.2% .

For comparison, we gave the same photometry used to infer SOM-based photo- z s to the template fitting code *Le Phare* (Arnouts et al. 1999; Ilbert et al. 2006). We find a scatter σ_{NMAD} of 2.9%, an outlier fraction of 3.8%, and bias after removing outliers of -1.3% . The scatter is significantly higher than that with the SOM-based photo- z , while the outlier rate is slightly lower. Importantly, the bias is substantially worse. This illustrates the performance gain achieved simply by averaging high-quality photo- z estimates (derived from overlapping deep data, potentially with additional bands) at each point in the lower-dimensional color space of a wide-area survey such as *Euclid* or *WFIRST*.

5.2. Serendipitous Sources

We detected 437 sources that serendipitously landed in a slit with the primary source (“serendips”). Of these, 51 were already in the literature with high-confidence redshifts. The agreement with literature values is nearly exact aside from three sources. We believe we understand these mismatches and trust our results in those cases.

A number of our serendipitous detections fall very close ($\lesssim 1''$) to the main source of interest, highlighting an important issue for photometric redshift calibration: the possibility of obtaining a secure redshift for the wrong source. In fact, in some of these cases it is difficult or impossible to determine which source is the primary and which is the serendipitous source. This issue was also noted by Brinchmann et al. (2017),

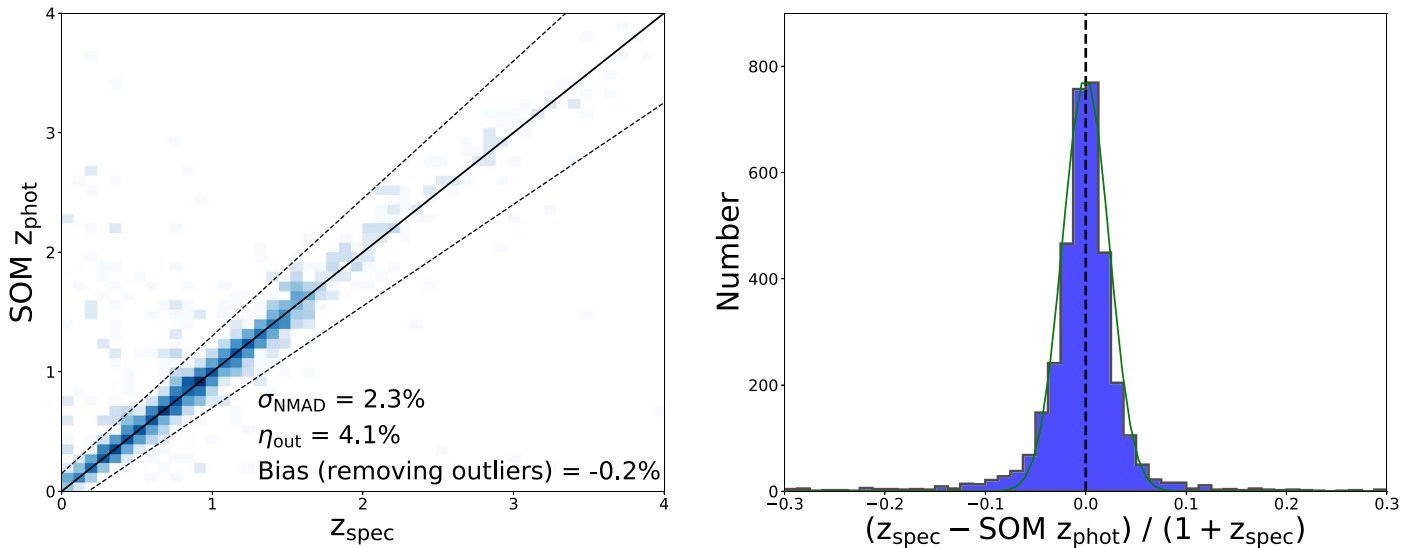


Figure 6. Performance of the SOM method on the DR1+2 data. We find an outlier fraction of 4.1%, a scatter of 2.3%, and a bias after removing outliers of -0.2% . Also, it is worth noting that our outliers are mostly low-redshift sources that scattered to high SOM z rather than the reverse, which may be an observational bias, as we are unable to measure redshifts for many of the outliers on the other side, with true redshifts at $z > 1.5$. The green line on the right panel is a Gaussian centered at 0 with $\sigma = 2.3\%$.

Table 3
List of Observing Nights

UT Date	Code	Instrument	# Masks	Observers	Notes
2016 Sep 29	N06-L	LRIS	3	AP,AS,DS	0"6 seeing; not photometric
2016 Oct 2	N07-D	DEIMOS	1	DM,AP	moisture/cloud cover, 0"9 seeing when open
2016 Oct 3	N08-D	DEIMOS	3	DM,AP	moisture/cloud cover, 0"8 seeing when open
2016 Nov 27	N09-L	LRIS	1	PB,MH,ARi,DS	cloudy, variable seeing (1"2–2"0)
2016 Nov 28	N10-D	DEIMOS	6.5	AS,DS	cloudy, variable seeing (1"0–2"0)
2016 Nov 29	N11-D	DEIMOS	5	AS,DS	clear, 0"65 seeing
2016 Nov 30	N12-D	DEIMOS	2.5	AS,DS	intermittent closures due to fog, flurries; 1"2 seeing
2016 Dec 1	N13-D	DEIMOS	...	AS,DS	lost to snow
2016 Dec 7	N14-D	DEIMOS	...	PB,AG,BS,DS	lost to recovery from winter storm
2016 Dec 8	N15-D	DEIMOS	1	AG,MJ,BS,DS	high humidity, cirrus; closed most of night
2016 Dec 20	N16-D	DEIMOS	...	DS	[1/2 night]; lost to ice-covered dome
2017 Jan 2	N17-D	DEIMOS	5	DS	photometric; 0"6–1"0 seeing
2017 Jan 5	N18-D	DEIMOS	5	JC,NH,AS	photometric, windy, poor seeing (>1")
2017 Jan 6	N19-D	DEIMOS	3	JC,NH,AS	1/2 night lost to high humidity
2017 Jan 27	N20-D	DEIMOS	4.5	ARe,DS,AW	photometric, 1"0 seeing
2017 Jan 27	N21-L	LRIS	5	ARe,DS,AW	"
2017 Jan 30	N22-D	DEIMOS	4.5	ARe,AW	photometric, 0"75 seeing
2017 Mar 31	N23-D	DEIMOS	1	JCh,JCo,NH	poor, high humidity, intermittent closures
2017 Apr 1	N24-D	DEIMOS	3.5	JCo,NH	photometric, 0"9 seeing
2017 Apr 1	N25-L	LRIS	2	JCh,DS	"
2017 Apr 2	N26-D	DEIMOS	2.5	JCo,NH	photometric, 1"0 seeing
2017 Apr 2	N27-L	LRIS	2	JCh	"
2017 Apr 15	N28-M	MOSFIRE	3	NH,DM,DS	photometric, 0"7 seeing
2017 Apr 16	N29-M	MOSFIRE	4	NH,DM,DS	photometric, 0"6 seeing

Note. Observers (alphabetical by last name): PB—Peter Boorman, AG—Audrey Galametz, JCh—Jason Chu, JCo—Judith Cohen, MH—Marianne Heida, NH—Nina Hernitschek, MJ—Marziye Jafariyazani, DM—Daniel Masters, BM—Bahram Mobasher, AP—Andreas Plazas, ARe—Alessandro Rettura, ARi—Adric Riedel, BS—Behnam Darvish Sarvestani, AS—Adam Stanford, DS—Daniel Stern, AW—Anna Weigel.

who found that up to a few percent of secure emission-line redshifts in deep surveys can be spurious, due to a background source being blended with the target of interest.

In any case it is clear that such sources will have blended photometry, and should likely be considered invalid for redshift calibration purposes. We summarize the close serendipis in Table 4, and illustrate one example in which two sources completely overlap in Figure 7. In that case two redshifts are

clearly evident, but one could imagine cases in which a single secure but spurious emission-line redshift is obtained for the primary source due to an overlapping galaxy.

5.3. Duplicate Observations

We (unintentionally) obtained duplicate high-confidence redshifts for 71 sources, providing a useful check on the consistency

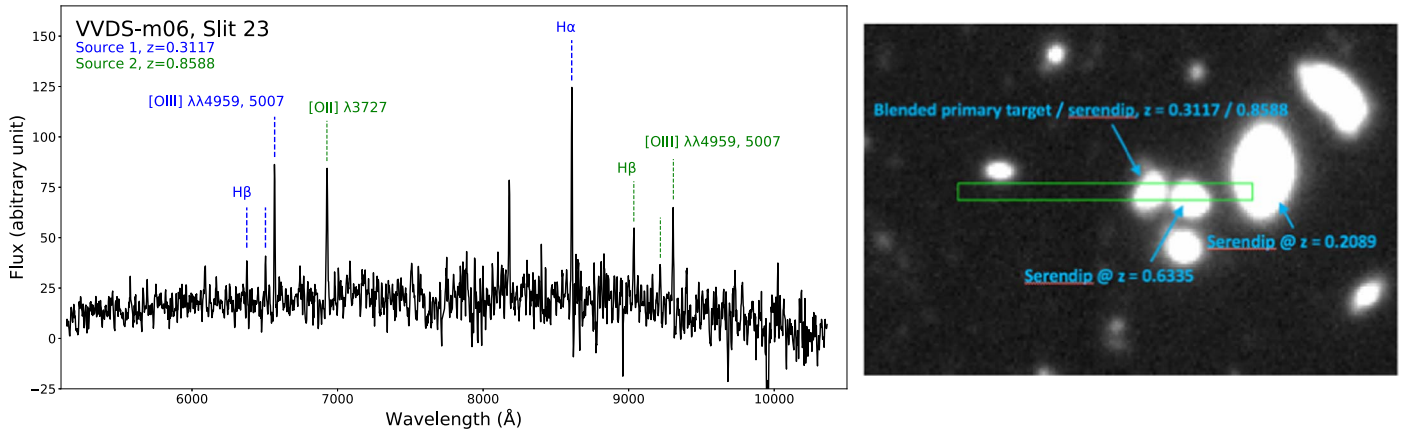


Figure 7. Example in which we clearly detect two emission-line redshifts for what appears to be a single source. This slit is particularly busy as there are an additional two serendipitous sources at $z = 0.6335$ and $z = 0.2089$ (indicated on the CFHTLS image on the right, with DEIMOS $1''$ width slit overlaid) that were detected; these spectra are not shown in the 1D extraction on the left. In the spectrum shown, the two redshifts reveal the problematic nature of the source. However, it is easy to imagine more pathological cases for which there is only one emission-line redshift detected and incorrectly attributed to the primary target. In any case, as there is clearly blended photometry for this source, similar ones should likely be excluded from calibration samples.

Table 4
Close Serendipitous Detections, Falling Within $1''$ of the Primary Target

Mask	Slit	Primary Target Name	Primary Spec- z	Serendip Spec- z	Offset
VVDS-m01	83	VVDS-45179	1.2477	1.2480	$0''00$
EGS-H-2hr3	6	EGS-336001	1.5624	1.7120	$0''00$
VVDS-m22	67	VVDS-186226	0.4635	1.4900	$0''00$
VVDS-m06	23	VVDS-439390	0.3117	0.8588	$0''00$
EGS-4h1	58	EGS-312294	2.8651	1.5250	$0''00$
EGS-4h1	4	EGS-305620	1.4168	0.7322	$0''01$
EGS-4h1	25	EGS-298760	0.4723	0.8775	$0''01$
COSMOS-5h3	64	COSMOS-296536	0.9890	1.1605	$0''01$
COSMOS-5h3	5	COSMOS-293140	0.7493	0.9665	$0''01$
COSMOS-6h	87	COS-100	1.5746	0.7375	$0''02$
COSMOS-1h2	78	COSMOS-166492	1.3604	1.4165	$0''02$
COSMOS-m22	61	COSMOS-263650	1.3413	0.9970	$0''12$
COSMOS-6h	38	COS-980010	1.6202	0.8337	$0''22$
EGS-H-2hr5	4	EGS-394269	1.5812	1.3597	$0''25$
COSMOS-6h	85	COS-999227	1.2182	0.8367	$0''29$
COSMOS-m12	27	COSMOS-490417	1.4051	0.4745	$0''35$
EGS-4h2	17	EGS-372214	1.2711	1.1722	$0''38$
COSMOS-m21	78	COSMOS-238677	1.1551	1.2177	$0''41$
EGS-4h2	43	EGS-353596	1.6282	0.7286	$0''44$
VVDS-m25	18	VVDS-271560	0.3728	1.5569	$0''55$
VVDS-m02	68	VVDS-94232	0.9616	0.7872	$0''63$
VVDS-m04	75	VVDS-261586	0.6941	0.6346	$0''66$
COSMOS-m28	53	COSMOS-460081	0.8918	0.8332	$0''68$
VVDS-m14	46	VVDS-144620	0.6213	0.6215	$0''70$
COSMOS-m24	82	COSMOS-324794	0.7317	0.7253	$0''72$
EGS-4h1	42	EGS-317641	0.8442	0.9774	$0''72$
COSMOS-m17	39	COSMOS-105578	1.1781	0.4723	$0''73$
EGS-4h2	86	EGS-359810	0.6786	1.2090	$0''74$
VVDS-m12	66	VVDS-215721	1.1173	0.8511	$0''74$
EGS-4h2	9	EGS-362393	1.3213	0.9630	$0''75$
VVDS-m01	29	VVDS-56665	0.9600	0.9004	$0''77$
COSMOS-m33	22	COSMOS-965712	0.2236	1.4478	$0''83$
COSMOS-m28	71	COSMOS-451219	0.1013	1.2030	$0''83$
VVDS-m05	41	VVDS-344788	0.4372	0.6962	$0''91$
EGS-4h2	7	EGS-373437	1.7616	0.3345	$0''91$
VVDS-m07	65	VVDS-499386	0.8773	0.3455	$0''97$

and precision of our redshift results. We found no inconsistent redshift results, and our redshifts are precise to $\lesssim 1 \times 10^{-4}$; the median value of $\Delta z / (1 + \bar{z})$ between duplicate Spec- z s is

1.1×10^{-4} . Note that the duplicate results are published in the catalog, while the numbers quoted for the overall survey are for the unique sources in the sample.

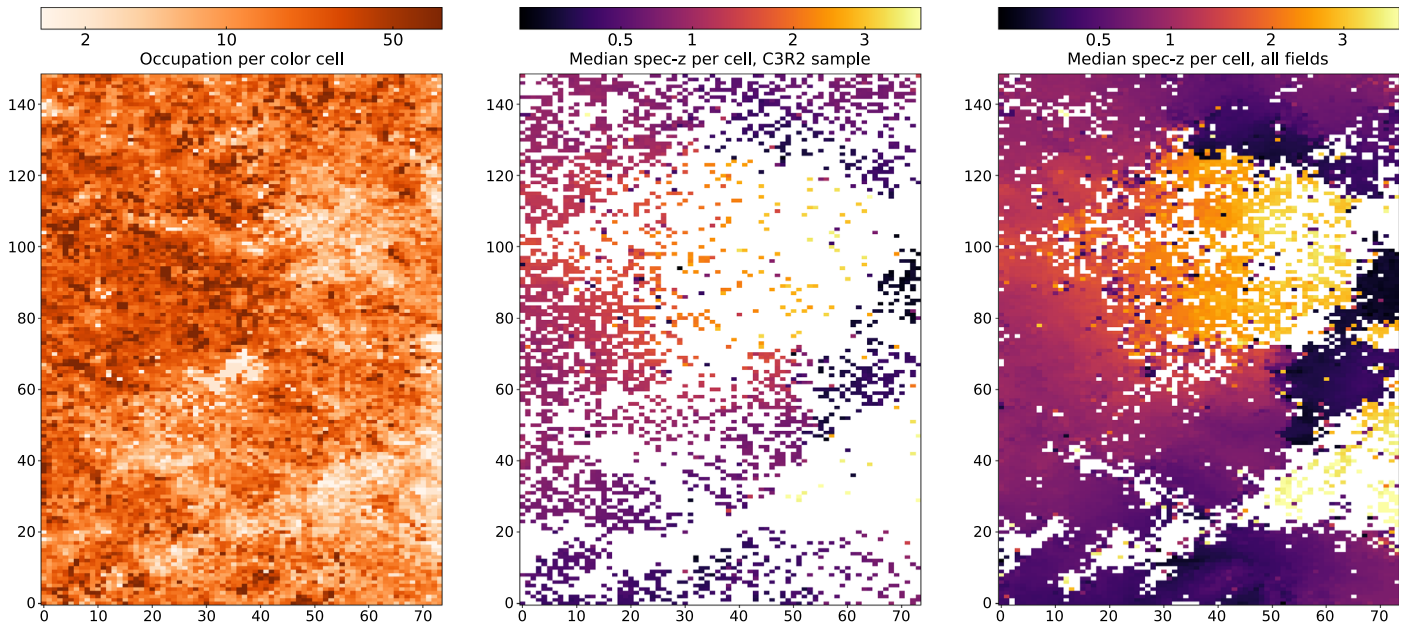


Figure 8. Left: occupation density of galaxies on the SOM. The distribution is clearly not uniform, reflecting the different sky density of galaxies in different parts of the *Euclid*/*WFIRST* color space. Center: C3R2 coverage of the color space. C3R2 has successfully observed $>35\%$ of the color cells. Right: the current total coverage of the SOM, incorporating C3R2 with spectra from numerous other surveys. Roughly 76% of color cells are covered, while $\sim 85\%$ of galaxies live within calibrated cells. Comparison with the occupation plot on the left shows that the remaining cells strongly correlate with less occupied regions of the galaxy color space.

5.4. Assessing the Photo- z Outliers

We examined the 130 outliers, or those sources with a secure redshift that differed from the predicted SOM-based redshift by $>15\%$. These fall in a range of categories: $\sim 25\%$ have an individual photo- z estimates more in line with the Spec- z , hinting at a true degeneracy in the color–redshift relation when limited to the *Euclid*/*WFIRST* color space; $\sim 25\%$ can be understood as rare objects (low-mass stars, quasars, extremely strong line emitters) with correspondingly unusual colors; while another $\sim 20\%$ have unusual colors due to blending with a nearby galaxy. The remaining $\sim 30\%$ seem to be either true outliers for which both the SOM- z and photo- z are incorrect, or problems with our redshift assignment. In fact, we found 14 cases for which the assigned redshift or quality flag was incorrect, either due to a mistake in the original assessment of the spectrum or in the process of reconciling and cataloging the results. We modified these accordingly.¹⁸ This analysis highlights the necessity of using great care in developing the “gold sample” of galaxies to use in calibrating photo- z for cosmology.

5.5. Spectroscopic Failures

Unfortunately, we cannot achieve 100% redshift success for faint galaxies. We therefore made an attempt to understand our spectroscopic failures and potential biases in the data. We consider only spectra from good weather nights, defined as $\leq 1''$ seeing with photometric conditions. We targeted a total of 4240 sources under these conditions in DR1+2. Of these, 1287 (30%) were “failures,” meaning we could not recover a secure redshift from the reduced spectrum.

¹⁸ One might worry that modifying redshifts “by hand” after the fact could be injecting a bias in the results. However, we are concerned with producing the highest quality data product possible. We therefore feel it is justified if obvious mistakes are uncovered; moreover, the total number of cases amounts to only 0.4% of the overall sample.

We focus on the good-weather failures in the COSMOS field, for which we have the most accurate photometric redshifts, ancillary data, and predicted exposure times from our calculator. This leaves 671 sources. Of these, 186 were assigned low-confidence ($Q = 2$ or $Q = 1$) redshifts, 286 have a failure code of -91 , indicating they were too faint to yield a secure redshift, and 149 have a code of -92 , indicating a reasonable continuum detection but nevertheless no redshift determination. The remaining 50 have code of -93 or -94 , meaning there was a reduction problem, so they are not of great interest for this analysis.

Of the sources too faint to yield a secure redshift, 71% were predicted by our exposure time calculator to take longer than the actual integration; in other words, we expected to fail for these sources. For the other 29% the situation is less clear, but it is likely that our exposure time calculator was optimistic. For the failures for which we had a good continuum detection, a full 66% were not expected to yield a secure redshift for the given exposure time. Of the others, $\sim 38\%$ were classified as quiescent, indicating that we have systematic difficulty (as expected) getting redshifts for passive galaxies in comparison to star-forming ones.

A potentially worrying failure mode for calibration arises from sources at the redshift boundary of what can easily be done with DEIMOS or other optical spectrographs. Nearly 50% of the sources for which we measured continuum but no redshift have a photo- z near 1.5, where the $[\text{O II}]\lambda 3727$ line can easily be missed if it happens to fall off the red end of the detector. One can imagine a bias toward lower redshifts when calibrating such galaxies.

6. Calibration Progress

We performed some tests to get a sense of the state of redshift calibration. We will address the issue of large-scale structure variations within the relatively small calibration fields in more detail in a separate paper.

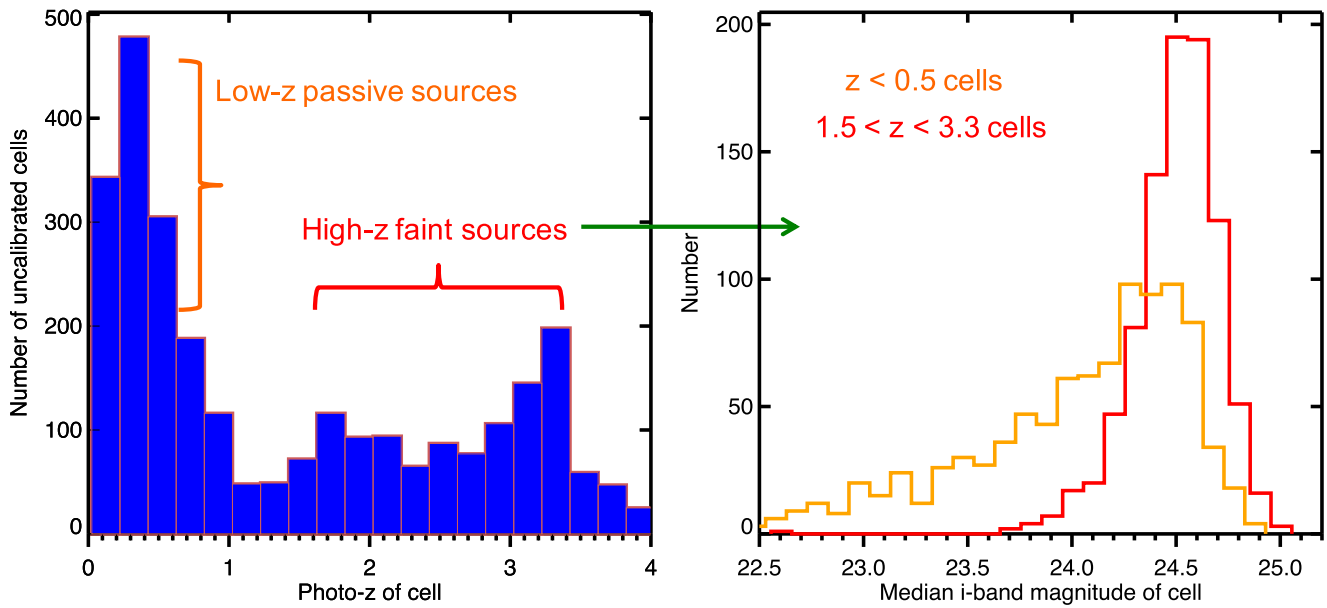


Figure 9. Summary of the presently uncalibrated cells. Most of the cells correspond to relatively low-density parts of the color space. The low- z peak represents mostly passive galaxies for which obtaining a secure redshift is difficult (as well as some star-forming but rare sources). The high- z peak are galaxies for which obtaining a redshift with an optical spectrograph is difficult, and are primarily quite faint, as shown in the right plot.

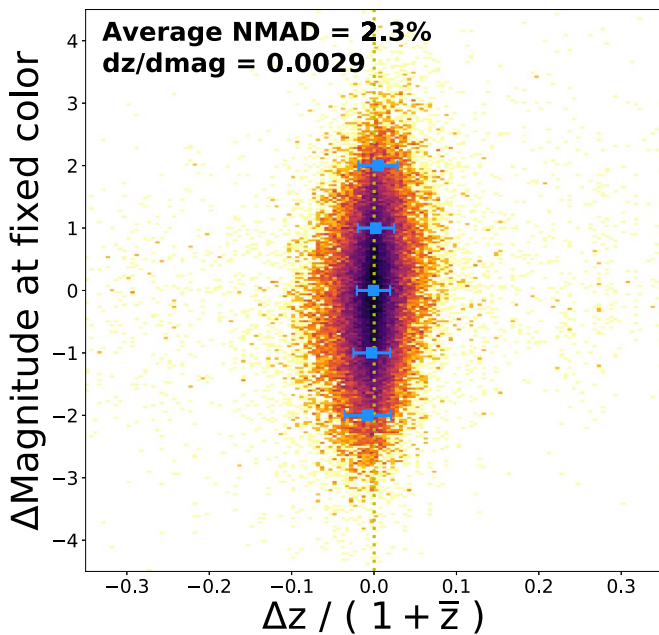


Figure 10. Test of the importance of galaxy brightness for redshift inference for the *Euclid*/*WFIRST* color space. For each unique pair of Spec- z galaxies at fixed color (in the same SOM cell), we plot the difference in i -band magnitude vs. the difference in measured redshift. As can be seen, there is a weak dependence on magnitude, which we quantify with a fit to the running medians (in blue, with scatter bars, computed in slices of Δmag of width 0.2 across the distribution) as ~ 0.0029 change in $\Delta z / (1 + \bar{z})$ per magnitude. The scatter reflects the redshift uncertainty at fixed color, which depends on both the photometric error and intrinsic uncertainty in the color–redshift relation. This result has important implications for the *WFIRST* calibration (see Hemmati et al. 2018), for which there are significant numbers of optically faint sources with similar colors as brighter galaxies.

6.1. Color Space Coverage

When we consider spectra from all of our fields, we are currently covering $\sim 76\%$ of the cells with high-quality spectra, which “calibrates” $\sim 86\%$ of sources (Figure 8). The majority

of the uncalibrated cells also are those with fewer galaxies, so in principle they are less important to the overall calibration. For comparison, prior to the C3R2 survey the color space coverage estimated in M15 was $\sim 50\%$. The C3R2 sample alone has covered over 35% of the color space, much of which was previously uncharted.

It may be noted that the fraction of calibrated cells we quote may be dependent on the total number of cells, which is a hyperparameter of the SOM. We argue that the cells of the current SOM are fine enough that increasing the resolution further would not improve our understanding of the $P(z|C)$ relation at the depth of *Euclid*. When we say that a galaxy is “calibrated” we are really saying that we have at least one spectroscopic redshift for a galaxy with colors that are indistinguishable from that galaxy at the depth of *Euclid*.

6.2. What Are the Remaining Uncalibrated Galaxies?

A key question for calibration is what galaxies are we still missing, and why? The majority seem to be a combination of low- z quiescent or star-forming but rare galaxies, and galaxies at $1.5 \lesssim z \lesssim 3$ for which DEIMOS and other optical spectrographs have difficulty in obtaining secure redshifts. The redshift and magnitude distributions of the uncalibrated cells are summarized in Figure 9. To fully complete the coverage would require deep spectroscopy on low-sky-density sources. Upcoming wide-area multiobject fiber spectrographs (e.g., the Prime Focus Spectrograph on Subaru; Tamura et al. 2016) may be well-suited for this.

6.3. Magnitude Dependence

Important for photo- z calibration is the extent to which the magnitude of a galaxy carries additional information about its redshift, relative to its observed colors. This is particularly relevant if it is found that the galaxies successfully targeted with spectroscopy are systematically brighter than average at a fixed point in the survey color space.

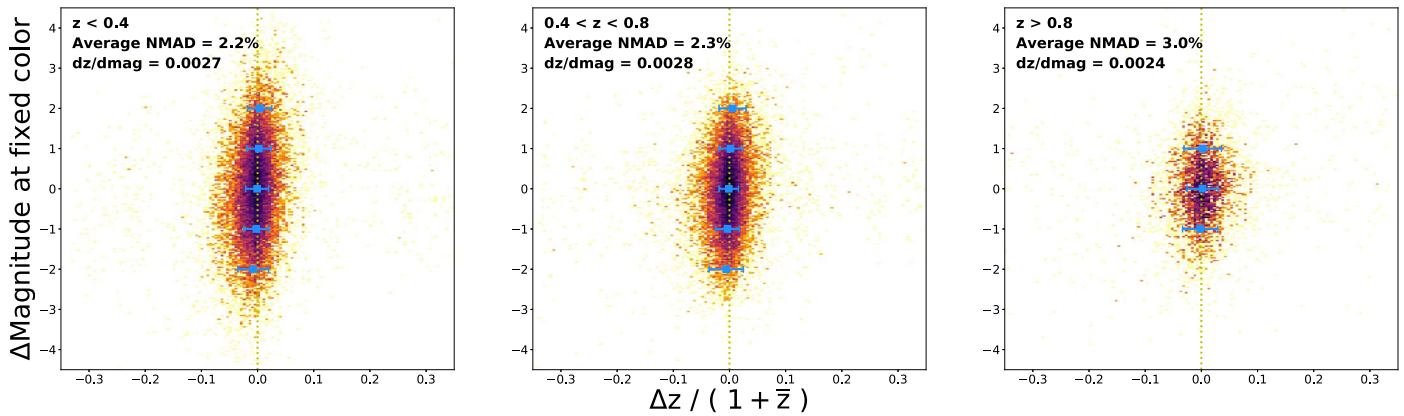


Figure 11. Same plot as Figure 10, but this time splitting by redshift. The scatter and slope of the relation are virtually unchanged in different redshift bins. The weak but significant variation of redshift with magnitude at fixed color appears to be intrinsic, likely explained by subtle variations in color with mass/metallicity counterbalanced by slightly different redshifts.

We performed a test based on our full spectroscopic calibration sample to address this issue, comprising spectra from surveys such as zCOSMOS (Lilly et al. 2007), DEEP2 (Newman et al. 2013), and VVDS (Le Fèvre et al. 2015), among others, in addition to the C3R2 spectra. There are many color cells in the SOM that contain multiple galaxies with high-confidence spectroscopic redshifts when considering all of these surveys. Therefore we take every unique pair of spectroscopic galaxies at fixed color in our sample, and examine the correlation between their difference in magnitude and difference in redshift. The result is shown in Figure 10.

The scatter in $\Delta z / (1 + \bar{z})$ in this figure tells us the uncertainty in the redshift at fixed color, both due to inherent uncertainty in the $P(z|C)$ relationship itself and photometric uncertainty. This value is $\sim 2.3\%$, in agreement with the scatter we infer for the SOM-based photometric redshifts. More importantly, we find a very weak (but non-zero) correlation between Δmag and $\Delta z / (1 + \bar{z})$ at fixed *Euclid*/*WFIRST* color. The relationship has a slope of 0.003 mag^{-1} . While small, this relation is at a level that may be of concern for cosmology. Further detailed analysis would be required to understand how best to calibrate for the effect. However, the relation appears stable across redshift, as illustrated in Figure 11. Moreover, we tested whether it can be ascribed to small color variations of galaxies within a given SOM cell. This does not seem to be the explanation, as we find that the colors do not seem to systematically vary with galaxy brightness at a fixed SOM cell. We are investigating this issue using simulations and it will be explored more in a subsequent paper.

6.4. Cosmic Variance

Because the calibration fields used by C3R2 are relatively small ($\sim 1\text{--}2 \text{ deg}^2$), cosmic variance will imprint a different $N(z)$ in each field than would be measured in wide-area surveys. This effect may impact the redshift calibration, and certainly would bias any $N(z)$ estimate drawn only from these fields, in comparison with the true $N(z)$ for a wide-area survey.

Two critical questions are raised. (1) Is the $P(z|C)$ relation itself unchanged across fields, regardless of variations in the relative numbers of galaxies at fixed color due to cosmic variance? (2) Is the SOM generated on a handful of deep fields sufficiently spanning the color space of galaxies?

We can get a sense of the cosmic variance in the fields by examining the density field in color space, $\rho(C)$, in VVDS-2h and COSMOS separately. As Figure 12 shows, roughly the same global density is found in each field, but with variations indicative of the different clustering in the fields. A simple assessment of whether the $P(z|C)$ relation is affected by this variation can be made by calibrating the relation with COSMOS only, then applying that solution to VVDS-2h. We performed this analysis and found a largely unchanged redshift results for the VVDS-2h sources; in other words, regardless of clustering, at fixed color the relation appears to be stable across fields. A more detailed analysis of the effect of cosmic variance on the calibration of $P(z|C)$ will be the subject of a future paper.

7. Summary

We have presented 3171 new redshifts obtained by the C3R2 survey. We have shown that the redshift calibration strategy for *Euclid* undertaken by C3R2 is making excellent progress, although it hinges strongly on obtaining highly homogeneous imaging across large deep fields. More extensive tests are required to ensure that we will meet the cosmology requirements. A key question is the extent to which cosmic variance will limit the utility of the redshift results in the deep fields when applying them to future wide surveys. We have also shown an empirical relation between magnitude difference and redshift at fixed *Euclid*/*WFIRST* color. This relation may prove important for extending the spectroscopic calibration of the $P(z|C)$ relation to deeper *WFIRST* and LSST sources for which obtaining spectroscopy will remain challenging into the 2020s.

Our results illustrate that there is a strong, mostly non-degenerate relationship between observed galaxy optical-through-near-IR colors and redshift, and therefore uncovering this relation directly via targeted spectroscopy is a reliable method to calibrate redshifts for the dark energy experiments to be conducted over the next decade. Moreover, the quality of the redshift solution derived using the median multi-band photometric redshifts at each point in the *Euclid*/*WFIRST* color space suggests that deep surveys overlapping wide-area surveys can be invaluable, particularly if they include more photometric bands than the wide survey. We emphasize that C3R2 is filling in regions of galaxy parameter space that are underrepresented in existing spectroscopic surveys. However, those surveys

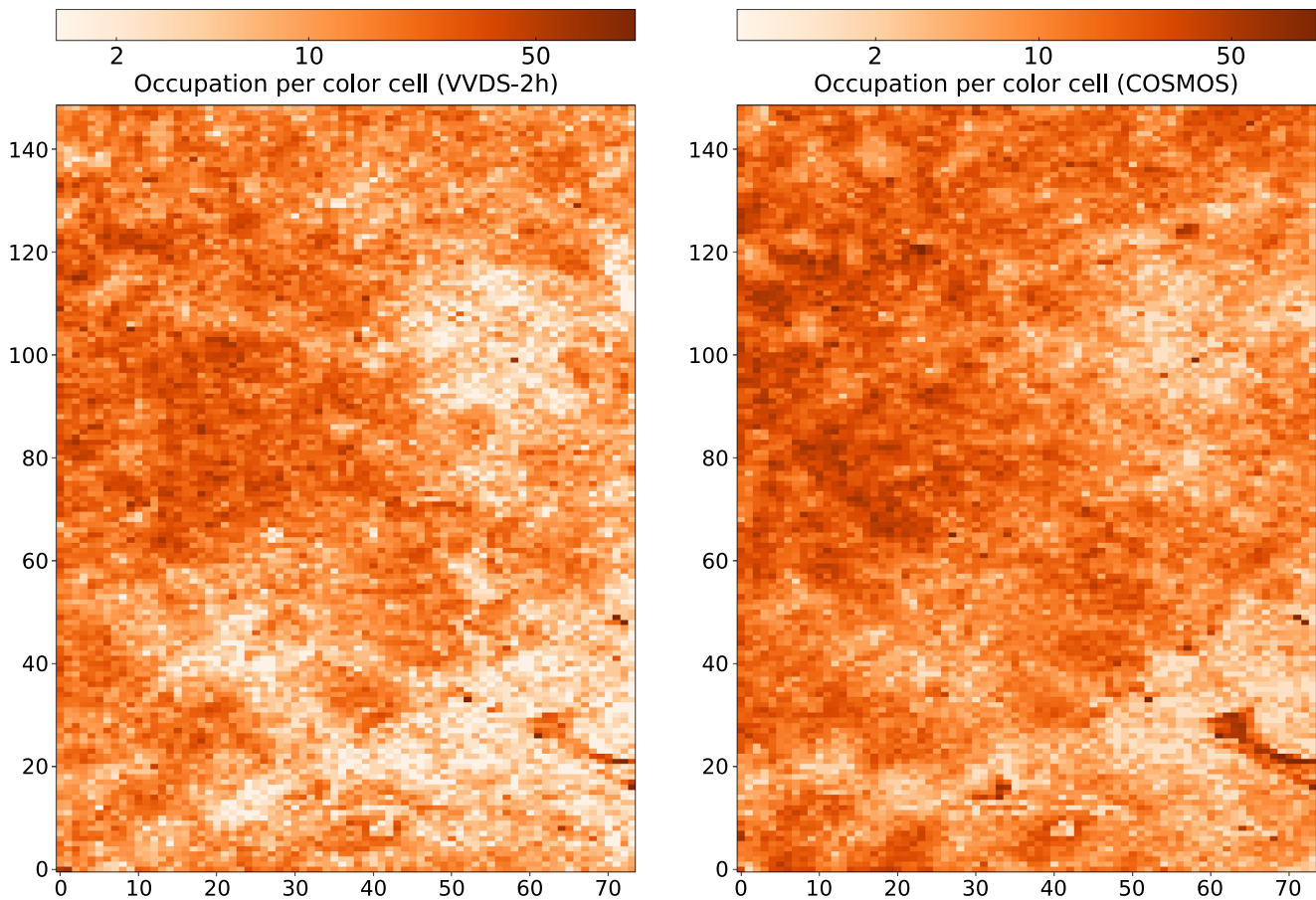


Figure 12. Comparison of relative occupation density of galaxies in color space in COSMOS vs. VVDS-2h. Variation of the fields is evident, and the median relative difference in occupation for a given cell of the color space is $\sim 50\%$. If, however, we rebin the map in 5×5 cells, the variance is much lower; at a median value of $\sim 25\%$ per color cell. Overall this illustrates the general similarity in frequency of colors in different fields, while also highlighting the impact of cosmic variance.

collectively have contributed hugely to mapping the galaxy color–redshift relation.

A key goal for the community interested in calibrating photometric redshifts for weak lensing cosmology should be to develop a homogenized database of *all* 1D/2D spectra taken to date from which all surveys can benefit. As we have shown, care is needed to avoid calibrating the $P(z|C)$ relation with ambiguous sources, nearby galaxies in projection, etc. These can be a sizable fraction particularly at the depths of the upcoming surveys, and thus a carefully curated database of reliable and well-vetted spectroscopy is needed.

We thank the anonymous referee for a thorough and constructive report that improved this manuscript. The research

was carried out at the Jet Propulsion Laboratory, California Institute of Technology, under a contract with the National Aeronautics and Space Administration. D.M., D.S., P.C., and J. R. acknowledge support by NASA ROSES grant 12-EUCLID12-0004. D.M. acknowledges support for this work from a NASA Postdoctoral Program Fellowship. This work was enabled by a NASA Keck grant.

©2018. All rights reserved.

Appendix

Here we summarize all of the observed slitmasks for this data release (Table 5), as well as a sample of the catalog of released redshifts (Table 6).

Table 5
List of Observed Slitmasks

Mask ID/Name	Night	R.A. (J2000)	Decl. (J2000)	PA ($^{\circ}$)	Exposure (s)
16B-L027/VVDS-m01	N06-L	2:24:54.5	-4:37:15	8.8	6 \times 1200
16B-L028/VVDS-m02	N06-L	2:24:52.8	-4:04:02	-20.1	6 \times 1200
16B-L029/VVDS-m03	N06-L	2:25:03.8	-4:07:43	158.5	3 \times 1200
16B-D030/VVDS-m03	N07-D	2:27:17.8	-4:40:03	90.0	6 \times 1200*
16B-D031/VVDS-m01	N08-D	2:27:18.0	-4:53:40	90.0	4 \times 1200* ^a
16B-D032/VVDS-m05	N08-D	2:27:22.4	-4:22:12	90.0	3 \times 1200*
16B-D033/VVDS-m04	N08-D	2:27:24.7	-4:28:54	90.0	6 \times 1200*
16B-L034/VVDS-m04	N09-L	2:27:11.0	-4:04:10	0.0	9 \times 1200
16B-D035/VVDS-m06	N10-D	2:27:16.2	-4:12:12	90.0	4 \times 1200
16B-D036/VVDS-m21	N10-D	2:24:49.8	-4:44:00	90.0	6 \times 1200
16B-D037/VVDS-m22	N10-D	2:24:50.5	-4:39:53	90.0	5 \times 1200
16B-D038/VVDS-m07	N10-D+N12-D	2:26:22.7	-4:04:00	90.0	2 \times 900 + 2 \times 1200
16B-D039/COSMOS-m11	N10-D	9:58:42.4	+2:37:37	90.0	4 \times 1200
16B-D040/COSMOS-m12	N10-D	9:58:42.8	+2:42:34	90.0	3 \times 1200
16B-D041/COSMOS-m13	N10-D	9:58:35.7	+2:45:47	90.0	2 \times 1200 + 900
16B-D042/VVDS-m08	N11-D	2:26:00.0	-4:11:55	90.0	3 \times 1200
16B-D043/VVDS-m01	N11-D	2:27:18.0	-4:53:40	90.0	9 \times 1200
16B-D044/VVDS-m23	N11-D	2:24:50.2	-4:36:00	90.0	5 \times 1200
16B-D045/COSMOS-m14	N11-D	9:59:55.3	+1:41:54	90.0	4 \times 1200
16B-D046/COSMOS-m21	N11-D	9:59:53.3	+2:10:00	90.0	7 \times 1200
16B-D047/VVDS-m09	N12-D	2:25:57.2	-4:20:18	90.0	2 \times 900
16B-D048/COSMOS-m16	N12-D	9:59:48.2	+1:49:05	90.0	3 \times 1200
16B-D049/VVDS-m10	N15-D	2:25:53.1	-4:28:36	90.0	2 \times 1200 + 1058
16B-D050/VVDS-m02	N17-D	2:27:20.3	-4:48:03	90.0	9 \times 1200
16B-D051/VVDS-m11	N17-D	2:26:01.1	-4:32:18	90.0	2 \times 1200 + 900
16B-D052/COSMOS-m15	N17-D	9:59:50.4	+1:46:00	90.0	4 \times 1200
16B-D053/COSMOS-m24	N17-D	9:59:52.4	+2:22:00	90.0	9 \times 1200
16B-D054/COSMOS-m17	N17-D	9:59:51.6	+1:54:32	90.0	4 \times 1200
16B-D055/VVDS-m12	N18-D	2:26:02.8	-4:36:12	90.0	3 \times 1200
16B-D056/VVDS-m24	N18-D	2:24:50.1	-4:32:24	90.0	5 \times 1200
16B-D057/COSMOS-m18	N18-D	9:59:56.5	+1:54:59	90.0	4 \times 1200
16B-D058/COSMOS-m22	N18-D	9:59:53.0	+2:14:00	90.0	6 \times 1200
16B-D059/COSMOS-m23	N18-D	9:59:52.4	+2:18:00	90.0	7 \times 1200
16B-D060/COSMOS-m27	N19-D	9:59:55.0	+2:35:00	90.0	5 \times 1200
16B-D061/COSMOS-m25	N19-D	10:00:17.3	+2:25:56	90.0	9 \times 1200
16B-D062/COSMOS-m28	N19-D	9:59:57.3	+2:37:54	90.0	3 \times 1200
16B-D063/VVDS-m13	N20-D	2:25:59.6	-4:40:09	90.0	3 \times 1200
16B-D064/VVDS-m14	N20-D	2:25:59.2	-4:43:50	90.0	2 \times 1150 + 1250
16B-D065/COSMOS-m19	N20-D	9:59:53.0	+2:01:56	90.0	3 \times 1200
16B-D066/COSMOS-6h	N20-D+N22-D	10:02:34.6	+2:48:01	90.0	18 \times 1200 + 1600
16B-D067/COSMOS-m32	N20-D	9:59:56.8	+2:45:12	90.0	3 \times 1200
16B-L068/VVDS-m7	N21-L	2:25:55.2	-4:13:42	148.4	6 \times 1200
16B-L069/VVDS-m5	N21-L	2:26:26.7	-4:42:45	1.7	3 \times 1200
16B-L070/COSMOS-m10	N21-L	10:01:01.7	+2:41:05	101.0	4 \times 1200 + 900
16B-L071/COSMOS-m13	N21-L	9:59:05.8	+1:45:13	178.4	9 \times 1200
16B-L072/COSMOS-m11	N21-L	10:00:00.2	+2:04:25	31.0	5 \times 1200
16B-L073/VVDS-m25	N22-D	2:24:49.8	-4:28:04	90.0	5 \times 1200 + 1150
16B-D074/COSMOS-m33	N22-D	10:01:07.8	+2:45:12	90.0	3 \times 1200
16B-D075/COSMOS-m34	N22-D	10:01:03.0	+2:41:00	90.0	3 \times 1200 + 1150
16B-D076/COSMOS-m39	N22-D	10:01:13.8	+2:21:02	90.0	7 \times 1200
17A-D077/COSMOS-5h1	N23-D+N24-D	10:01:41.9	+2:04:24	90.0	15 \times 1200
17A-D078/EGS-4h1	N23-D+N24-D	14:18:00.1	+52:46:00	90.0	13 \times 1200
17A-D079/COSMOS-1h1	N24-D	10:00:19.2	+2:15:21	90.0	4 \times 1200
17A-D080/COSMOS-1h2	N24-D	9:59:59.4	+2:02:44	90.0	3 \times 1200
17A-D081/EGS-4h2	N24-D+N26-D	14:17:59.8	+52:51:00	90.0	15800 ^b
17A-L082/COS-IriD/COS-5hr1	N25-L	10:01:43.8	+2:23:31	129.9	15 \times 1200
17A-L083/EGS-IriE/EGS-4hr1	N25-L	14:19:35.9	+53:05:23	-131.6	11 \times 1200
17A-D084/COSMOS-5h3	N26-D	9:59:46.8	+2:19:00	90.0	13 \times 1200
17A-D084/EGS-1h5	N26-D	14:18:00.3	+52:36:00	-147.1	1 \times 1800
17A-L085/COS-IriE/COS-5hr2	N27-L	10:01:29.1	+2:21:34	90.0	13 \times 1200

Table 5
(Continued)

Mask ID/Name	Night	R.A. (J2000)	Decl. (J2000)	PA ($^{\circ}$)	Exposure (s)
17A-L086/EGS-IriF/EGS-4hr2	N27-L	14:18:07.4	+53:02:06	-171.5	14 \times 1200
17A-M087/COSMOS-H-2hr3	N28-M	10:01:49.8	+2:36:02	-12.0	60 \times 120
17A-M088/EGS-H-2hr3	N28-M	14:17:30.9	+52:49:33	35.0	60 \times 120
17A-M089/EGS-H-2hr4	N28-M	14:19:00.4	+53:05:14	5.0	60 \times 120
17A-M090/COSMOS-H-2hr1	N29-M	9:58:33.7	+1:50:59	20.0	60 \times 120
17A-M091/COSMOS-H-1hr6	N29-M	10:01:29.9	+1:52:23	30.0	24 \times 120
17A-M092/EGS-H-2hr5	N29-M	14:17:01.8	+52:56:32	35.0	60 \times 120
17A-M093/EGS-H-2hr6	N29-M	14:20:11.1	+53:00:10	30.0	60 \times 120

Notes. “Night” column refers to observing code in second column of Table 1: night number, followed by letter indicating instrument used (D—DEIMOS, L—LRIS, M—MOSFIRE). R.A. and decl. refer to the mask center. Final column gives total number of slitlets in mask, total number of high-quality ($Q = 4$) redshifts measured, and the number of serendipitous sources with high-quality redshifts ($Q = 4$). * - Taken under poor conditions. See notes.

^a 3 hr mask abandoned during fifth exposure due to heavy cloud cover. Re-observed on N11-D as mask 16B-D043.

^b 4 \times 1200+5 \times 1800+2000.

Table 6
C3R2 Spectroscopic Redshift Results


ID	R.A. (J2000)	Decl. (J2000)	Mask	Slit	i mag	z	Qual.	Instr.	File
UDS-3583	02:17:30.65	-05:15:24.4	UDS-m1n1	1	23.4	0.7877	4.0	DEIMOS	spec1d.u-m1n1.001.UDS-3583.fits
UDS-10246	02:17:17.55	-05:13:06.9	UDS-m1n1	2	23.9	0.8028	4.0	DEIMOS	spec1d.u-m1n1.002.UDS-10246.fits
UDS-767	02:17:59.05	-05:16:21.2	UDS-m1n1	3	25.0	0.5558	4.0	DEIMOS	spec1d.u-m1n1.003.UDS-767.fits
UDS-7109	02:17:00.35	-05:14:15.4	UDS-m1n1	4	23.6	1.0314	3.0	DEIMOS	spec1d.u-m1n1.004.UDS-7109.fits
UDS-2276	02:17:52.83	-05:15:55.2	UDS-m1n1	5	22.9	0.9388	4.0	DEIMOS	spec1d.u-m1n1.005.UDS-2276.fits
UDS-8536	02:17:53.37	-05:13:40.3	UDS-m1n1	6	24.7	0.8619	4.0	DEIMOS	spec1d.u-m1n1.006.UDS-8536.fits
UDS-9784	02:17:56.80	-05:13:15.9	UDS-m1n1	9	23.6	0.8533	4.0	DEIMOS	spec1d.u-m1n1.009.UDS-9784.fits
UDS-10739	02:17:44.88	-05:12:58.7	UDS-m1n1	10	23.2	1.0594	4.0	DEIMOS	spec1d.u-m1n1.010.UDS-10739.fits
UDS-9730	02:17:32.64	-05:13:17.4	UDS-m1n1	12	23.8	1.0949	4.0	DEIMOS	spec1d.u-m1n1.012.UDS-9730.fits
...									

Note. Table 6 is published in its entirety in machine-readable format. A portion is shown here for guidance regarding its form and content. More detailed information is available in the header of the machine-readable table.

(This table is available in its entirety in machine-readable form.)


ORCID iDs

Daniel C. Masters  <https://orcid.org/0000-0001-5382-6138>


Daniel K. Stern  <https://orcid.org/0000-0003-2686-9241>

Judith G. Cohen  <https://orcid.org/0000-0002-8039-4673>

Peter L. Capak  <https://orcid.org/0000-0003-3578-6843>

Nina Hernitschek  <https://orcid.org/0000-0003-1681-0430>

Iary Davidzon  <https://orcid.org/0000-0002-2951-7519>

Jason D. Rhodes  <https://orcid.org/0000-0002-4485-8549>

Dave Sanders  <https://orcid.org/0000-0002-1233-9998>

Francisco Castander  <https://orcid.org/0000-0001-7316-4573>

References

- Aihara, H., Arimoto, N., Armstrong, R., et al. 2018, *PASJ*, 70, S4
- Arnouts, S., Cristiani, S., Moscardini, L., et al. 1999, *MNRAS*, 310, 540
- Benítez, N. 2000, *ApJ*, 536, 571
- Bertin, E. 2006, in ASP Conf. Ser. 351, *Astronomical Data Analysis Software and Systems XV*, ed. C. Gabriel et al. (San Francisco, CA: ASP), 112
- Bertin, E., Mellier, Y., Radovich, M., et al. 2002, in ASP Conf. Ser. 281, *Astronomical Data Analysis Software and Systems XI*, ed. D. A. Bohlender, D. Durand, & T. H. Handley (San Francisco, CA: ASP), 228
- Bielby, R., Hudelot, P., McCracken, H. J., et al. 2012, *A&A*, 545, A23
- Brammer, G. B., van Dokkum, P. G., & Coppi, P. 2008, *ApJ*, 686, 1503
- Brinchmann, J., Inami, H., Bacon, R., et al. 2017, *A&A*, 608, A3
- Capak, P., Aussel, H., Ajiki, M., et al. 2007, *ApJS*, 172, 99
- Carrasco Kind, M., & Brunner, R. J. 2013, *MNRAS*, 432, 1483
- Collister, A. A., & Lahav, O. 2004, *PASP*, 116, 345
- Davis, M., Guhathakurta, P., Konidaris, N. P., et al. 2007, *ApJL*, 660, L1
- de Jong, J. T. A., Verdoes Kleijn, G. A., Boxhoorn, D. R., et al. 2015, *A&A*, 582, A62
- de Jong, J. T. A., Verdois Kleijn, G. A., Erben, T., et al. 2017, *A&A*, 604, A134
- DES Collaboration, Abbott, T. M. C., Abdalla, F. B., et al. 2018, *PhRvD*, 98, 043526
- Galametz, A., Saglia, R., Paltani, S., Apostolokos, N., & Dubath, P. 2017, *A&A*, 598, A20
- Hemmati, S., Capak, P., Masters, D., et al. 2018, arXiv:1808.10458
- Hildebrandt, H., Viola, M., Heymans, C., et al. 2017, *MNRAS*, 465, 1454
- Huterer, D., Takada, M., Bernstein, G., & Jain, B. 2006, *MNRAS*, 366, 101
- Ilbert, O., Arnouts, S., McCracken, H. J., et al. 2006, *A&A*, 457, 841
- Ilbert, O., Capak, P., Salvato, M., et al. 2009, *ApJ*, 690, 1236
- Jarvis, M. J., Bonfield, D. G., Bruce, V. A., et al. 2013, *MNRAS*, 428, 1281
- Kohonen, T. 1982, *Biological Cybernetics*, Vol. 43, 59
- Laigle, C., McCracken, H. J., Ilbert, O., et al. 2016, *ApJS*, 224, 24
- Le Fèvre, O., Mellier, Y., McCracken, H. J., et al. 2004, *A&A*, 417, 839
- Le Fèvre, O., Tasca, L. A. M., Cassata, P., et al. 2015, *A&A*, 576, A79
- Lilly, S. J., Le Fèvre, O., Renzini, A., et al. 2007, *ApJS*, 172, 70

- Lima, M., Cunha, C. E., Oyaizu, H., et al. 2008, *MNRAS*, 390, 118
- Ma, Z., Hu, W., & Hutereu, D. 2006, *ApJ*, 636, 21
- Massey, P., & Gronwall, C. 1990, *ApJ*, 358, 344
- Masters, D., Capak, P., Stern, D., et al. 2015, *ApJ*, 813, 53
- Masters, D. C., Stern, D. K., Cohen, J. G., et al. 2017, *ApJ*, 841, 111
- McCracken, H. J., Milvang-Jensen, B., Dunlop, J., et al. 2012, *A&A*, 544, A156
- McCracken, H. J., Radovich, M., Bertin, E., et al. 2003, *A&A*, 410, 17
- McQuinn, M., & White, M. 2013, *MNRAS*, 433, 2857
- Ménard, B., Scranton, R., Schmidt, S., et al. 2013, arXiv:1303.4722
- Morrison, C. B., Hildebrandt, H., Schmidt, S. J., et al. 2017, *MNRAS*, 467, 3576
- Newman, J. A. 2008, *ApJ*, 684, 88
- Newman, J. A., Cooper, M. C., Davis, M., et al. 2013, *ApJS*, 208, 5
- Schmidt, S. J., Ménard, B., Scranton, R., Morrison, C., & McBride, C. K. 2013, *MNRAS*, 431, 3307
- Scoville, N., Aussel, H., Brusa, M., et al. 2007, *ApJS*, 172, 1
- Steidel, C. C., Rudie, G. C., Strom, A. L., et al. 2014, *ApJ*, 795, 165
- Tamura, N., Takato, N., Shimono, A., et al. 2016, *Proc. SPIE*, 9908, 99081M
- Troxel, M. A., MacCrann, N., Zuntz, J., et al. 2018, *PhRvD*, 98, 043528